International Journal of Computational Methods
Vol. 3, No. 4 (2006) 401–428


World Scientific
www.worldscientific.com

# A LINEARLY CONFORMING RADIAL POINT INTERPOLATION METHOD FOR SOLID MECHANICS PROBLEMS

G. R. LIU*, Y. LI† and K. Y. DAI‡

*Centre for Advanced Computations in Engineering Science*
*Department of Mechanical Engineering, National University of Singapore*
*9 Engineering Drive 1, Singapore, 119260*
**mpeliugr@nus.edu.sg*
†*yongli_scyl@hotmail.com*
‡*iesdky@nus.edu.sg*

M. T. LUAN§

†,§*School of Civil and Hydraulic Engineering, Dalian University of Technology*
*2 Linggong Road, Dalian, Liaoning 116024, P. R. China*
§*mtluan@dlut.edu.cn*

W. XUE

*Wenzhou University, Wenzhou, Zhejiang 325035, P. R. China*
*xw@wzu.edu.cn*

A linearly conforming radial point interpolation method (LC-RPIM) is presented for stress analysis of two-dimensional solids. In the LC-RPIM method, each field node is enclosed by a Voronoi polygon, and the displacement field function is approximated using RPIM shape functions of Kronecker delta function property created by simple interpolation using local nodes and radial basis functions augmented with linear polynomials to guarantee linear consistency. The system equations are then derived using the Galerkin weak form and nodal integration techniques, and the essential boundary conditions are imposed directly as in the finite element method. The LC-RPIM method is verified via various numerical examples and an extensive comparison study is conducted with the conventional RPIM, analytical approach and FEM. It is found that the presented LC-RPIM is more stable, more accurate in stress and more efficient than the conventional RPIM.

*Keywords*: Radial point interpolation method (RPIM); meshfree method; meshless method; interpolation function; stress analysis; radial basis function; nodal integration; gradient smoothing.

## 1. Introduction

The finite element method (FEM) has been well-established as a standard computational tool for solving a wide variety of complex mechanics problems [Liu (2003);

Liu and Gu (2005)]. However, there are some difficulties in applying FEM to simulate highly nonlinear problems involving extremely large deformation and crack propagation with arbitrary paths. The root of the problems is the utilization of the 'element' which is the inherent structure of FEM. Therefore, some meshfree methods or element free methods have been developed and achieved significant progress in recent years, such as the smooth particle hydrodynamics (SPH) method that uses integral representation of a function and particle approximation to create discretized system equations [Lucy (1977); Gingold and Monaghan (1977); Randles and Libersky (1996)], the element-free Galerkin (EFG) method [Belytschko *et al.* (1994), Lu *et al.* (1994), Belytschko *et al.* (1996)] that uses moving least squares (MLS) approximation and the Galerkin weak form, the reproducing kernel particle method (RKPM) that ensures the certain degree of consistency of the integral approximation by modifying integral kernel function [Liu *et al.* (1995)], the meshless local Petrov–Galerkin (MLPG) that uses the local Petrov-Galerkin weak form [Atluri and Zhu (1998); Atluri *et al.* (1999)], the point interpolation method (PIM) and radial point interpolation method (RPIM) based on both Galerkin weak form and Petrov-Galerkin weak form [Liu and Gu (2001); Wang and Liu (2002)]. Detailed descriptions and discussions on these meshfree methods can be found in [Liu (2003); Liu and Gu (2005)].

The RPIM has the following advantages:

(1) The shape function has the Kronecker delta property, which facilitates easy treatment of the essential boundary conditions.
(2) The moment matrix used in constructing shape functions is always invertible for irregular nodes.
(3) The polynomials can be exactly reproduced up to desired order by polynomial augmentation.

However, background cells must be used for Gaussian integration of the Galerkin weak form. In addition, the RPIM is not conforming unless the constraint weak form is used [Liu (2003)]. To make full use of the advantages of RPIM and at the same time to ensure conformability, a linearly conforming RPIM (LC-RPIM) is proposed in this work by means of gradient smoothing for field functions based on the nodal integration techniques [Chen *et al.* (2001); Chen *et al.* (2002)].

This paper is organized as follows. Section 2 reviews briefly the procedure of creating RPIM shape functions. Section 3 presents the equations for boundary value problems of mechanics and deduces its variational weak form as well as the resultant discrete system equations. In Sec. 4, the integration constraints are introduced to exactly reproduce a linear displacement field solution, and the average gradient of the field function is then given out. Section 5 performs an intensive study of several numerical examples solved using the proposed LC-RPIM, non-conforming RPIM (NC-RPIM), analytical formulae and the conventional FEM. Finally, some conclusions are made in the last section.

## 2. Interpolation Formulations

Radial point interpolation method (RPIM) is formulated based on the Galerkin weak form using shape functions of Kronecker delta function property created through an interpolation using local nodes and radial and polynomial basis functions. Such an interpolation is often used by many researchers for curve or surface fitting and function approximation [Golberg *et al.* (1996)]. The procedure of constructing RPIM shape functions is briefed as follows.

The function of a displacement component $u(\mathbf{x})$ is approximated using radial and polynomial basis functions in the form of

$$u(\mathbf{x}) = \sum_{i}^{n} R_i(\mathbf{x}) a_i + \sum_{j}^{m} P_j(\mathbf{x}) b_j = \mathbf{R}^{\mathrm{T}}(\mathbf{x})\mathbf{a} + \mathbf{P}^{\mathrm{T}}(\mathbf{x})\mathbf{b} \tag{1}$$

where $R_i(\mathbf{x})$ and $P_j(\mathbf{x})$ are radial and polynomial basis functions in two dimensional space $\mathbf{x}^{\mathrm{T}} = [x, y]$, $n$ is the number of field nodes in the local support domain of point $\mathbf{x}$, $m$ is the number of terms of polynomial basis functions, and $a_i$ and $b_j$ are coefficients for $R_i(\mathbf{x})$ and $P_j(\mathbf{x})$ respectively. These vectors are defined as

$$\begin{aligned} \mathbf{R}(\mathbf{x}) &= [R_1(\mathbf{x}), R_2(\mathbf{x}), R_3(\mathbf{x}), \ldots, R_n(\mathbf{x})]^{\mathrm{T}} \\ \mathbf{P}(\mathbf{x}) &= [P_1(\mathbf{x}), P_2(\mathbf{x}), P_3(\mathbf{x}), \ldots, P_m(\mathbf{x})]^{\mathrm{T}} \\ \mathbf{a} &= [a_1, a_2, a_3, \ldots, a_n]^{\mathrm{T}} \\ \mathbf{b} &= [b_1, b_2, b_3, \ldots, b_m]^{\mathrm{T}} \end{aligned} \tag{2}$$

The radial basis function $R_i(\mathbf{x})$ has the following general form

$$R_i(\mathbf{x}) = R_i(x, y) = R(r_i) \tag{3}$$

where $r_i$ is a distance between the interpolating point $\mathbf{x}$ and field node $\mathbf{x}_i$, which can be represented as

$$r_i = [(x_i - x)^2 + (y_i - y)^2]^{\frac{1}{2}} \tag{4}$$

The polynomial basis vector $\mathbf{P}(\mathbf{x})$ has the following form for two dimensional domains.

$$\mathbf{P}(\mathbf{x}) = [1, x, y, x^2, xy, y^2, \ldots]^{\mathrm{T}} \tag{5}$$

The coefficient vectors $\mathbf{a}$ and $\mathbf{b}$ are determined by enforcing the displacement of all the $n$ field nodes within the local support domain to satisfy Eq. (1). Following a lengthy but straightforward procedure given by [Liu (2003)], we can arrive at

$$u(\mathbf{x}) = \mathbf{N}(\mathbf{x})\mathbf{U}_s, \tag{6}$$

where the vector $\mathbf{N}(\mathbf{x})$ contains $n$ shape functions:

$$\mathbf{N}(\mathbf{x}) = [N_1(\mathbf{x}), N_2(\mathbf{x}), \ldots, N_k(\mathbf{x}), \ldots, N_n(\mathbf{x})]^{\mathrm{T}}, \tag{7}$$

in which $N_k(\mathbf{x})$ is the shape function for the $k$th node given by [Liu (2003)]:

$$N_k(\mathbf{x}) = \sum_i^n R_i(\mathbf{x})\mathbf{S}_{aik} + \sum_j^m P_j(\mathbf{x})\mathbf{S}_{bjk}, \tag{8}$$

where $\mathbf{S}_{aik}$ is the $(i,k)$ element of matrix $\mathbf{S}_a = \mathbf{R}_M^{-1} - \mathbf{R}_M^{-1}\mathbf{P}_M\mathbf{S}_b$, and $\mathbf{S}_{bjk}$ is the $(j,k)$th element of matrix $\mathbf{S}_b = (\mathbf{P}_M^T\mathbf{R}_M^{-1}\mathbf{P}_M)^{-1}\mathbf{P}_M^T\mathbf{R}_M^{-1}$. The moment matrices $\mathbf{P}_M$ and $\mathbf{R}_M$ are, respectively, given by

$$\mathbf{P}_M = \begin{bmatrix} P_1(\mathbf{x}_1) & P_2(\mathbf{x}_1) & \cdots & P_m(\mathbf{x}_1) \\ P_1(\mathbf{x}_2) & P_2(\mathbf{x}_2) & \cdots & P_m(\mathbf{x}_2) \\ \vdots & \vdots & \ddots & \vdots \\ P_1(\mathbf{x}_n) & P_2(\mathbf{x}_n) & \cdots & P_m(\mathbf{x}_n) \end{bmatrix} \tag{9}$$

$$\mathbf{R}_M = \begin{bmatrix} R_1(\mathbf{x}_1) & R_2(\mathbf{x}_1) & \cdots & R_n(\mathbf{x}_1) \\ R_1(\mathbf{x}_2) & R_2(\mathbf{x}_2) & \cdots & R_n(\mathbf{x}_2) \\ \vdots & \vdots & \ddots & \vdots \\ R_1(\mathbf{x}_n) & R_2(\mathbf{x}_n) & \cdots & R_n(\mathbf{x}_n) \end{bmatrix} \tag{10}$$

The RPIM shape functions $N_i(\mathbf{x})$ obtained through the above procedure have following properties regardless of particular form of radial basis function:

(a) Shape functions have Kronecker delta function properties, that is

$$N_i(\mathbf{x} = \mathbf{x}_j) = \begin{cases} 1, & i = j, \quad j = 1, 2, \ldots, n, \\ 0, & i \neq j, \quad i, j = 1, 2, \ldots, n. \end{cases} \tag{11}$$

(b) Shape functions are partitions of unity:

$$\sum_i^n N_i(\mathbf{x}) = 1. \tag{12}$$

(c) When $m = 3$, the shape functions have the property of linear polynomial reproducibility:

$$\sum_i^n N_i(\mathbf{x})\mathbf{x}_i = \mathbf{x}. \tag{13}$$

(d) Shape functions have simple derivatives such as

$$\begin{Bmatrix} \dfrac{\partial N_k}{\partial x} \\ \dfrac{\partial N_k}{\partial y} \end{Bmatrix} = \sum_i^n \frac{\partial R_i}{\partial r_i}\frac{\mathbf{S}_{aik}}{r_i}\begin{Bmatrix} x - x_i \\ y - y_i \end{Bmatrix} + \sum_j^m \mathbf{S}_{bjk}\begin{Bmatrix} \dfrac{\partial P_j}{\partial x} \\ \dfrac{\partial P_j}{\partial y} \end{Bmatrix}. \tag{14}$$

There are many types of radial basis functions [Golberg *et al.* (1996); Liu (2003)]. In this work the multiquadrics radial basis function (MQ-RBF) with arbitrary real shape parameters is used that has the form of [Liu (2003)]

$$R(r_i) = (r_i^2 + \alpha_c^2 d_c^2)^q, \tag{15}$$

where $\alpha_c$ and $q$ are real shape parameters to be determined by numerical testing, $d_c$ is a characteristic length that is related to the nodal spacing in the local support domain of the interested point $\mathbf{x}$, and $d_c = \min\{r_i\}(r_i > 0,\ i = 1, \ldots, n)$ in this work.

## 3. Variational Form

In this section, standard boundary value equations for plane problems in solid mechanics are first introduced, and then the variational principle is established by defining potential functional. Finally the discrete system equations of the presented LC-RPIM method are derived.

### 3.1. *Weak form equations for 2D elasticity*

(1) The static equilibrium equation (strong form) governing the solid defined in domain $\boldsymbol{\Omega}$ can be given as

$$\mathbf{B}^{\mathrm{T}} \left( \frac{\partial}{\partial x}, \frac{\partial}{\partial y} \right) \boldsymbol{\sigma} + \mathbf{b} = 0 \quad \text{in } \boldsymbol{\Omega} \tag{16}$$

where $\boldsymbol{\sigma} = [\sigma_{xx}, \sigma_{yy}, \tau_{xy}]^{\mathrm{T}}$ is a vector of stress and $\mathbf{b}$ represents body force density. The operator $\mathbf{B}^{\mathrm{T}}(\frac{\partial}{\partial x}, \frac{\partial}{\partial y})$ has following form

$$\mathbf{B}^{\mathrm{T}} \left( \frac{\partial}{\partial x}, \frac{\partial}{\partial y} \right) = \begin{bmatrix} \dfrac{\partial}{\partial x} & 0 & \dfrac{\partial}{\partial y} \\ 0 & \dfrac{\partial}{\partial y} & \dfrac{\partial}{\partial x} \end{bmatrix}. \tag{17}$$

(2) At an arbitrary point the strain-displacement relation is given as

$$\boldsymbol{\varepsilon} = \mathbf{B} \left( \frac{\partial}{\partial x}, \frac{\partial}{\partial y} \right) \mathbf{u}, \tag{18}$$

in which $\boldsymbol{\varepsilon} = [\varepsilon_{xx}, \varepsilon_{yy}, \varepsilon_{xy}]^{\mathrm{T}}$ is strain vector, $\mathbf{u} = [u, v]^{\mathrm{T}}$ consists of displacement components.

(3) The constitutional equation for the material is given as

$$\boldsymbol{\sigma} = \mathbf{D}\boldsymbol{\varepsilon}, \tag{19}$$

where $\mathbf{D}$ is a matrix of elastic constants of the material. For elastic plane stress problems it is represented with Young's modulus $E$ and Poisson's ratio $\nu$ as

$$\mathbf{D} = \frac{E}{1-\nu^2}\begin{bmatrix} 1 & \nu & 0 \\ \nu & 1 & 0 \\ 0 & 0 & \dfrac{1-\nu}{2} \end{bmatrix}. \tag{20}$$

For plane strain problems, Eq. (20) holds after substituting $E$ and $\nu$ with $E/(1-\nu^2)$ and $\nu/(1-\nu)$, respectively.

(4) Boundary conditions

The displacement boundary condition can be given as

$$\mathbf{u} = \bar{\mathbf{u}} \quad \text{on } \Gamma_{\mathrm{u}}, \tag{21}$$

where $\bar{\mathbf{u}}$ is a specified displacement at boundary $\Gamma_{\mathrm{u}}$.

The traction boundary condition is given as

$$\mathbf{T} = \mathbf{B}^{\mathrm{T}}(n_x, n_y)\boldsymbol{\sigma} = \bar{\mathbf{T}} \quad \text{on } \Gamma_{\mathrm{T}} \tag{22}$$

in which $\bar{\mathbf{T}}$ is a given traction at boundary $\Gamma_{\mathrm{T}}$ and $\mathbf{n}^{\mathrm{T}} = [n_x \quad n_y]$ is the outward normal vector of the traction boundary.

### 3.2. *Variation principle*

By applying virtual displacement $\delta\mathbf{u}$ under the current configure with given boundary conditions, the virtual potential energy $\delta\Pi^{\mathrm{e}}$ and virtual work done by external force $\delta W^{\mathrm{ext}}$ are respectively given as follows

$$\delta\Pi^{\mathrm{e}} = \int_{\Omega} (\delta\boldsymbol{\varepsilon})^{\mathrm{T}} d\Omega = \int_{\Gamma} (\delta\mathbf{u})^{\mathrm{T}}\mathbf{B}^{\mathrm{T}}(n_x, n_y)\boldsymbol{\sigma}\, d\Gamma - \int_{\Omega} (\delta\mathbf{u})^{\mathrm{T}}\mathbf{B}^{T}\left(\frac{\partial}{\partial x}, \frac{\partial}{\partial y}\right)\boldsymbol{\sigma}\, d\Omega \tag{23}$$

$$\delta W^{\mathrm{ext}} = \int_{\Gamma_T} (\delta\mathbf{u})^{\mathrm{T}}\bar{\mathbf{T}}\, d\Gamma + \int_{\Omega} (\bar{\mathbf{u}})^{\mathrm{T}}\mathbf{b}\, d\Omega \tag{24}$$

Since the virtual work done by external force $\delta W^{\mathrm{ext}}$ equals the virtual potential energy $\delta\Pi^{\mathrm{e}}$ according to the virtual work principle, we have

$$\int_{\Omega} (\delta\mathbf{u})^{\mathrm{T}}\left(\mathbf{B}^{\mathrm{T}}\left(\frac{\partial}{\partial x}, \frac{\partial}{\partial y}\right)\boldsymbol{\sigma} + \mathbf{b}\right) d\Omega - \int_{\Gamma_{\mathrm{T}}} (\delta\mathbf{u})^{\mathrm{T}}(\mathbf{B}^{\mathrm{T}}(n_x, n_y)\boldsymbol{\sigma} - \bar{\mathbf{T}})\, d\Gamma = 0. \tag{25}$$

From Eq. (25) it is evident that Eqs. (16) and (22) can be derived because that virtual displacement $\delta\mathbf{u}$ is arbitrary.

The potential energy functional $\Pi$ can be represented as

$$\Pi = \frac{1}{2}\int_{\Omega} \boldsymbol{\varepsilon}^{\mathrm{T}}\mathbf{D}\boldsymbol{\varepsilon}\, d\Omega - \int_{\Omega} \mathbf{u}^{\mathrm{T}}\mathbf{b}\, d\Omega - \int_{\Gamma_{\mathrm{T}}} \mathbf{u}^{\mathrm{T}}\bar{\mathbf{T}}\, d\Gamma \tag{26}$$

The variational (or weak) form of the system can now be presented as

$$\delta\Pi = \int_{\Omega} (\delta\boldsymbol{\varepsilon})^{\mathrm{T}}\mathbf{D}\boldsymbol{\varepsilon}\, d\Omega - \int_{\Omega} (\delta\mathbf{u})^{\mathrm{T}}\mathbf{b}\, d\Omega - \int_{\Gamma_{\mathrm{T}}} (\delta\mathbf{u})^{\mathrm{T}}\,\bar{\mathbf{T}} d\Gamma = 0. \tag{27}$$

### 3.3. *Discrete governing equations*

Equation (27) can now be discretized using numerical nodal integration at the field nodes [Chen *et al.* (2002)] and RPIM shape functions, which gives

$$\delta\Pi = (\delta\mathbf{U})^{\mathrm{T}} \left\{ \left( \sum_{i=1}^{n_{\mathrm{G}}} \tilde{\mathbf{B}}_i^{\mathrm{T}}\mathbf{D}\tilde{\mathbf{B}}_i A_i \right) \mathbf{U} - \left[ \sum_{i=1}^{n_{\mathrm{G}}} \mathbf{N}_i^{\mathrm{T}}\mathbf{b}A_i + \sum_{i=1}^{n_{\mathrm{T}}} \mathbf{N}_i^{\mathrm{T}}\bar{\mathbf{T}}_i L_i \right] \right\} \tag{28}$$

where $U = [u_1, v_1, u_2, v_2, \ldots, u_{n_{\mathrm{G}}}, v_{n_{\mathrm{G}}}]^{\mathrm{T}}$, $n_{\mathrm{G}}$ represents number of all field nodes, $n_{\mathrm{T}}$ is the number of nodes on $\Gamma_{\mathrm{T}}$; $A_i$ and $L_i$ are, respectively, area and boundary length associated with the $i$th node. Note the summations represent the assembly procedure similar to that in the conventional FEM, and

$$\mathbf{N}_i = \mathbf{N}(\mathbf{x}_i) = [\mathbf{N}_{i1}\ \mathbf{N}_{i2}\ \cdots\ \mathbf{N}_{ik}\ \cdots\ \mathbf{N}_{in_i}] \tag{29}$$

$$\tilde{\mathbf{B}}_i = \mathbf{B}\left(\frac{\partial}{\partial x}, \frac{\partial}{\partial y}\right)\mathbf{N}(\mathbf{x}_i) = [\tilde{\mathbf{B}}_{i1}\ \tilde{\mathbf{B}}_{i2}\ \cdots\ \tilde{\mathbf{B}}_{ik}\ \cdots\ \tilde{\mathbf{B}}_{in_i}] \tag{30}$$

where $\mathbf{N}_{ik} = \mathbf{N}_k(\mathbf{x}_i) = \begin{bmatrix} N_{ik} & 0 \\ 0 & N_{ik} \end{bmatrix}$ and $\tilde{\mathbf{B}}_{ik} = \begin{bmatrix} \frac{\partial N_{ik}}{\partial x} & 0 \\ 0 & \frac{\partial N_{ik}}{\partial y} \\ \frac{\partial N_{ik}}{\partial y} & \frac{\partial N_{ik}}{\partial x} \end{bmatrix}^{\mathrm{T}}$, $N_{ik} = N_k(\mathbf{x}_i)$ represents the value of the shape function of the $k$th node (in the local support domain) at the $i$th node, and $n_i$ represents the number of nodes included in the local support domain of the $i$th node.

Invoking $\delta\Pi = 0$ for any $\delta\mathbf{U}$, we can obtain a set of linear system algebraic equations

$$\left( \sum_{i=1}^{n_{\mathrm{G}}} \tilde{\mathbf{B}}_i^{\mathrm{T}}\mathbf{D}\tilde{\mathbf{B}}_i A_i \right)\mathbf{U} = \sum_{i=1}^{n_{\mathrm{G}}} \mathbf{N}_i^{\mathrm{T}}\mathbf{b}A_i + \sum_{i=1}^{n_{\mathrm{T}}} \mathbf{N}_i^{\mathrm{T}}\bar{\mathbf{T}}_i L_i \tag{31}$$

Equation (31) can be rewritten in a matrix form of

$$\mathbf{K}\mathbf{U} = \mathbf{F} \tag{32}$$

where

$$\mathbf{K} = \sum_{i=1}^{n_{\mathrm{G}}} \mathbf{K}_i \tag{33}$$

$$\mathbf{F} = \sum_{i=1}^{n_{\mathrm{G}}} \mathbf{F}_{\mathrm{b}i} + \sum_{i=1}^{n_{\mathrm{T}}} \mathbf{F}_{\mathrm{T}i} \tag{34}$$

$$\mathbf{K}_i = \tilde{\mathbf{B}}_i^{\mathrm{T}} \mathbf{D} \tilde{\mathbf{B}}_i A_i \tag{35}$$

$$\mathbf{F}_{\mathrm{b}i} = \mathbf{N}_i^{\mathrm{T}} \mathbf{b}_i A_i \tag{36}$$

$$\mathbf{F}_{\mathrm{T}i} = \mathbf{N}_i^{\mathrm{T}} \bar{\mathbf{T}}_i L_i \tag{37}$$

## 4. Integration Constraint and Gradient Smoothing

The convergence of the numerical solution for a partial differential equation is determined by the approximation of the field variables and the numerical integration of the weak form. RPIM shape functions with linear consistency can be obtained by including complete linear polynomial basis functions ($m = 3$). The linearly consistency in the RPIM shape functions does not, however, necessarily guarantee a linear exactness of the solution obtained by its weak form due to the conformability. Constraints associated with the nodal integration are required to ensure a linearly conformability in RPIM.

### 4.1. *Integration constraint*

For a given linear displacement field ignoring body force density $\mathbf{b}$ and displacement boundary, substituting stress constant $\boldsymbol{\sigma} = \boldsymbol{\sigma}^{\mathrm{c}}$ and traction $\bar{\mathbf{T}} = \mathbf{B}^{\mathrm{T}}(n_x, n_y)\boldsymbol{\sigma}^{\mathrm{c}}$ into Eq. (31), we have [Bonet and Kulasegaram (2002); Chen *et al.* (2001)]

$$\left( \sum_{i=1}^{n_{\mathrm{G}}} \tilde{\mathbf{B}}_i^{\mathrm{T}} A_i \right) \boldsymbol{\sigma}^{\mathrm{c}} = \left( \sum_{i=1}^{n_{\mathrm{T}}} \mathbf{N}_i^{\mathrm{T}} \mathbf{B}^{\mathrm{T}}(n_{ix}, n_{iy}) L_i \right) \boldsymbol{\sigma}^{\mathrm{c}}. \tag{38}$$

Since $\boldsymbol{\sigma}^{\mathrm{c}}$ is arbitrary, the above equation is true as long as

$$\sum_{i=1}^{n_{\mathrm{G}}} \tilde{\mathbf{B}}_i^{\mathrm{T}} A_i = \sum_{i=1}^{n_{\mathrm{T}}} \mathbf{N}_i^{\mathrm{T}} \mathbf{B}^{\mathrm{T}}(n_{ix}, n_{iy}) L_i, \tag{39}$$

or more general form

$$\sum_{j=1}^{n_i^{\mathrm{T}}} A_j \nabla N_{ji} = \sum_{k=1}^{n_i^{\mathrm{B}}} L_k N_{ki} \mathbf{n}_k, \tag{40}$$

where $n_i^{\mathrm{T}}$ and $n_i^{\mathrm{B}}$, respectively, represent nodal number in the influence domain of the $i$th field node $\tilde{\Omega}_i$ and on its boundary $\partial\tilde{\Omega}_i$.

It is noted that if the $i$th field node is in the interior of the domain, or specifically $\partial\tilde{\Omega}_i \cap \Gamma = \phi$, the right-hand side of this expression will vanish.

Only if the constraint given in Eq. (40) is satisfied can the RPIM obtain exact linear solution, and hence it will pass the standard linear patch test. Unfortunately, the condition cannot usually be met. Note that Eq. (40) is simply the nodal integration

version of the following continuous form:

$$\int_{\tilde{\Omega}_i} \nabla N_i(\mathbf{x}) d\Omega = \int_{\partial\tilde{\Omega}_i} \mathbf{n}(\mathbf{x}) N_i(\mathbf{x}) d\Gamma \tag{41}$$

Equation (41) is always satisfied as a result of the divergence theorem (or Gaussian theorem). Consequently, the reason for failing to satisfy Eq. (40) is due to the error introduced by nodal integration procedure using the standard gradient of displacement interpolation in Eq. (14) during the variational formation. Constraint given in Eq. (40) has already been arrived at by others for other meshfree methods [Bonet and Kulasegaram (2002); Chen *et al.* (2001)].

### 4.2. *Gradient smoothing*

To satisfy Eq. (40), a smoothing operation to the gradient of the field function is performed as follows [Chen *et al.* (2001); Chen *et al.* (2002)]:

$$\nabla^h \mathbf{u}(\mathbf{x}_i) = \int_{\Omega_i} \nabla \mathbf{u}(\mathbf{x}) \Phi(\mathbf{x} - \mathbf{x}_i) d\Omega. \tag{42}$$

Using integration by parts, Eq. (42) can be rewritten as

$$\nabla^h \mathbf{u}(\mathbf{x}_i) = \int_{\Gamma_i} \mathbf{n}(\mathbf{x}) \mathbf{u}(\mathbf{x}) \Phi(\mathbf{x} - \mathbf{x}_i)\, d\Gamma - \int_{\Omega_i} \mathbf{u}(\mathbf{x}) \nabla \Phi(\mathbf{x} - \mathbf{x}_i) d\Omega \tag{43}$$

where $\Phi$ is a smoothing function, $\Omega_i$ is the representative domain of the $i$th field node and $\Gamma_i$ is its boundary, as shown in Fig. 1.

For simplicity a piecewise constant function is used:

$$\Phi(\mathbf{x} - \mathbf{x}_i) = \begin{cases} \dfrac{1}{A_i} & \mathbf{x} \in \Omega_i; \\ 0 & \mathbf{x} \notin \Omega_i. \end{cases} \tag{44}$$

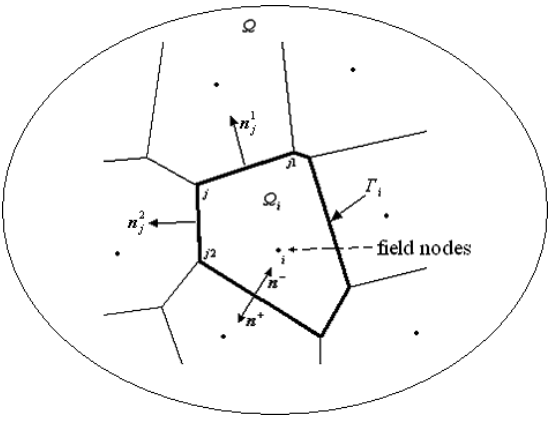


Fig. 1. Example of Voronoi diagram in a 2D domain.

Substituting Eq. (44) into Eq. (43), we obtain

$$\nabla^h \mathbf{u}(\mathbf{x}_i) = \frac{1}{A_i} \int_{\Gamma_i} \mathbf{n}(\mathbf{x})\mathbf{u}(\mathbf{x}) d\Gamma. \tag{45}$$

Using the trapezoidal rule of integration, Eq. (45) can also be given in a efficient form as

$$\nabla^h \mathbf{u}(\mathbf{x}_i) = \frac{1}{2A_i} \sum_{j=1}^{n_i^{\Gamma V}} \left(L_j^1 \mathbf{n}_j^1 + L_j^2 \mathbf{n}_j^2\right) \mathbf{u}\left(\mathbf{x}_j^V\right) \tag{46}$$

where $n_i^{\Gamma V}$ is the vertex number of the Voronoi diagram of the $i$th node, $L_j^1$ and $L_j^2$ are respectively lengths of two edges between the $j$th and $j1$th vertexes, and the $j$th and $j2$th vertexes, $\mathbf{n}_j^1$ and $\mathbf{n}_j^2$ are the corresponding outward normal vectors, as shown in Fig. 1.

Using the RPIM shape functions, the average smoothed gradient matrix $\bar{\mathbf{B}}(\mathbf{x}_i)$ can be given as

$$\bar{\mathbf{B}}(\mathbf{x}_i) = \frac{1}{2A_i} \sum_{j=1}^{n_i^{\Gamma V}} \left(L_j^1 \mathbf{n}_j^1 + L_j^2 \mathbf{n}_j^1\right) \mathbf{N}(\mathbf{x}_j^V). \tag{47}$$

Considering $n^+ = -n^-$ for any internal edge, the integration of the gradient matrix $\bar{\mathbf{B}}_i(\mathbf{x})$ for the $i$th nodes can be given as

$$\sum_{j=1}^{n_i^{\mathrm{T}}} \bar{\mathbf{B}}_i(\mathbf{x}_j) A_j = \frac{1}{2} \sum_{k=1}^{n_i^{\mathrm{BE}}} L_k^{\mathrm{E}} \mathbf{n}_k^{\mathrm{E}} (N_i(\mathbf{x}_k^{\mathrm{EV1}}) + N_i(\mathbf{x}_k^{\mathrm{EV2}})) \tag{48}$$

where $n_i^{\mathrm{BE}}$ is the number of Voronoi edges on boundary of the influence domain for the $i$th node, $L_k^{\mathrm{E}}$ and $\mathbf{n}_k^{\mathrm{E}}$ are the length and outward normal vector of the $k$th Voronoi edge, $\mathbf{x}_k^{\mathrm{EV1}}$ and $\mathbf{x}_k^{\mathrm{EV2}}$ are its two end points correspondingly.

It is obvious that the above equation is the discrete form of Eq. (41) which is the necessary conditions to reproduce the constant stress field.

## 5. Numerical Examples

An intensive numerical study is conducted using a number of examples to validate the proposed LC-RPIM. In these examples, the RPIM shape functions is constructed using MQ-RBF and complete linear polynomial functions ($m = 3$) are included to ensure linear consistency in the local displacement approximation. When computing the discrete system matrices, two integration schemes are used for comparison: (1) For the non-conforming RPIM (NC-RPIM), background cells are used and the integration is performed using $5 \times 5$ Gaussian points for each cell. The strain matrix is calculated via the standard gradient of RPIM shape functions given in Eq. (14), and the shape parameters used in the MQ-RBF are $\alpha_c = 4$ and $q = 1.03$; (2) For the proposed linearly conforming RPIM (LC-RPIM), nodal integration is used and the strain matrix is computed using the average gradient

given in Eq. (47). The numerical results are compared with those obtained using FEM with four-node isoparametric elements, and analytical solution whenever it is possible.

For qualitative error analysis, the following two relative error indicators for displacement and energy error are used:

$$error_{\mathrm{d}} = \sqrt{\int_{\Omega} [(u_{\mathrm{exact}} - u_{\mathrm{num}})^2 + (v_{\mathrm{exact}} - v_{\mathrm{num}})^2] d\Omega \Big/ \int_{\Omega} [u_{\mathrm{exact}}^2 + v_{\mathrm{exact}}^2] d\Omega}, \tag{49}$$

$$error_{\mathrm{e}} = \sqrt{\int_{\Omega} [(\boldsymbol{\varepsilon}_{\mathrm{exact}} - \boldsymbol{\varepsilon}_{\mathrm{num}})^{\mathrm{T}} \mathbf{D} (\boldsymbol{\varepsilon}_{\mathrm{exact}} - \boldsymbol{\varepsilon}_{\mathrm{num}})] d\Omega \Big/ \int_{\Omega} [\boldsymbol{\varepsilon}_{\mathrm{exact}}^{\mathrm{T}} \mathbf{D} \boldsymbol{\varepsilon}_{\mathrm{exact}}] d\Omega}, \tag{50}$$

where $u$ and $v$ are respectively the displacements in $x$ and $y$ directions, and $\boldsymbol{\varepsilon}$ is the vector of strains. The subscripts "exact" and "num" stand for the exact analytical solutions and the numerical solutions obtained using NC-RPIM, LC-RPIM or FEM.

Here the dimension of the support domain $d$ of a point of interest is expressed as follows.

$$d = \alpha_{\mathrm{s}} d_0 \tag{51}$$

where $d_0$ is the minimum dimension of the support domain including at least three nearest nodes for the interested point and $\alpha_{\mathrm{s}}$ is a dimensionless size of the support domain.

### 5.1. *Patch test*

The first numerical example is the standard patch test. A patch of 1 m × 1 m with both regularly and irregularly distributed 121 field nodes is used as shown in Fig. 2.

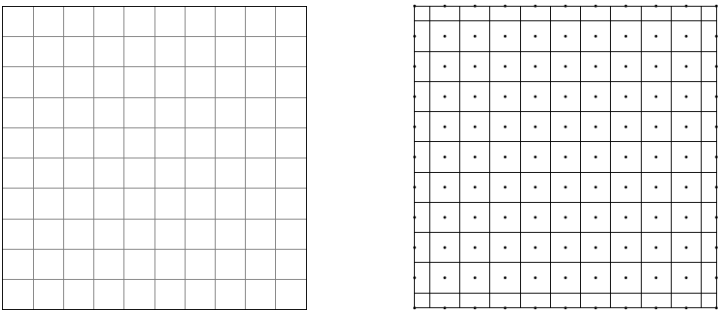

(a) (b)

Fig. 2. A patch with 121 field nodes. (a) Background integration cells for conventional RPIM. (b) Regular nodal distribution and the Voronoi diagrams. (c) Irregular nodal distribution and the Voronoi diagrams ($\alpha_{ir} = 0.4$).

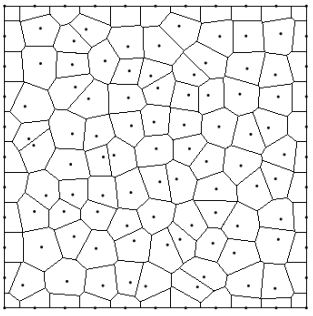

(c)

Fig. 2. (*Continued*)

The background cells shown in Fig. 2(a) are used for the Gaussian integrations for NC-RPIM.

The irregular nodes are created by altering the coordinates of the regular nodes using the following equation.

$$\begin{cases} x' = x + \Delta x \cdot r_{\mathrm{c}} \cdot \alpha_{ir}, \\ y' = y + \Delta y \cdot r_{\mathrm{c}} \cdot \alpha_{ir}, \end{cases} \tag{52}$$

where $\Delta x$ and $\Delta y$ are, respectively, the initial nodal spacing in the $x$ and $y$ direction, $r_{\mathrm{c}}$ is a computer generated random number between $-1.0$ to 1.0, and $\alpha_{\mathrm{ir}}$ is the irregularity factor.

In this standard test, the displacements are prescribed on all four outside boundaries by the linear functions of $u = x$ and $v = y$. The material parameters of the patch are $E = 1.0$ and $\nu = 0.25$, and the plane stress problem is considered. Satisfaction of the patch test requires that the displacements obtained by a numerical method at any interior point satisfy the same linear functions, the strains and stresses are constant in the entire patch.

### 5.1.1. *Effect of shape parameters $\alpha_{\mathrm{c}}$ and $q$*

In this investigation, regularly distributed nodes with the support domain of $\alpha_{\mathrm{s}} = 2.5$ are used. First, with the change of parameter $\alpha_{\mathrm{c}}$ at three different values of the parameter $q$ including 0.5, 1.03 and 1.3, the relative errors of displacement and energy obtained are plotted in Fig. 3(a). It is observed that the displacement and energy accuracies of the proposed method are about order of $10^{-14}$ within the machine accuracy when the parameter $\alpha_{\mathrm{c}}$ is less than 1.0 for $q = 0.5$ and $q = 1.3$, and 0.2 for $q = 1.03$. Within the bounds of the parameter $\alpha_{\mathrm{c}}$, the accuracies of displacement and energy are almost constant. Next, the shape parameter $\alpha_{\mathrm{c}}$ is fixed at three values 0.1, 1.0 and 4.0, while the shape parameter $q$ changes. The relative errors of the displacement and energy are computed and plotted in Fig. 3(b). It is observed again that the displacement and energy accuracies of the present method

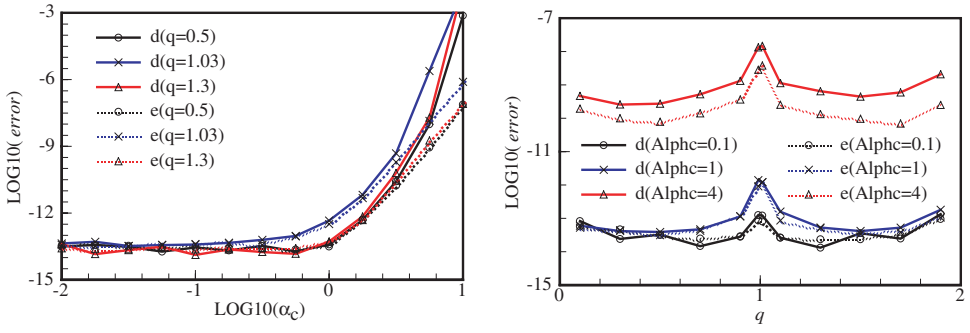


(a) (b)

Fig. 3. Relative error in the standard patch tests using LC-RPIM ($\alpha_s = 2.5$) with regular nodes. (a) Effect of $\alpha_c$. (b) Effect of $q$.

are very stable except in the neighbor of the singular point ($q$ is integer) for the MQ-BRF function. The accuracies are much higher for smaller parameter $\alpha_c$. Both errors are of the same order of $10^{-14}$ (near the machine accuracy) for $\alpha_c = 0.1$ and $\alpha_c = 1.0$. However, they are of the order of $10^{-11}$ for $\alpha_c = 4.0$. It implies that the shape parameter of the MQ-RBF should be selected properly to assure passing the patch test. In the following computations, $\alpha_c = 0.1$ and $q = 0.5$ are used in the MQ-RBF for constructing the RPIM shape functions in the LC-RPIM.

### 5.1.2. *Effect of the dimension of the support domain and the irregularity of nodal distribution*

In this study, the computed relative displacement and energy errors are plotted in Fig. 4(a) for the patch test with regular nodes and varying the support domain. It

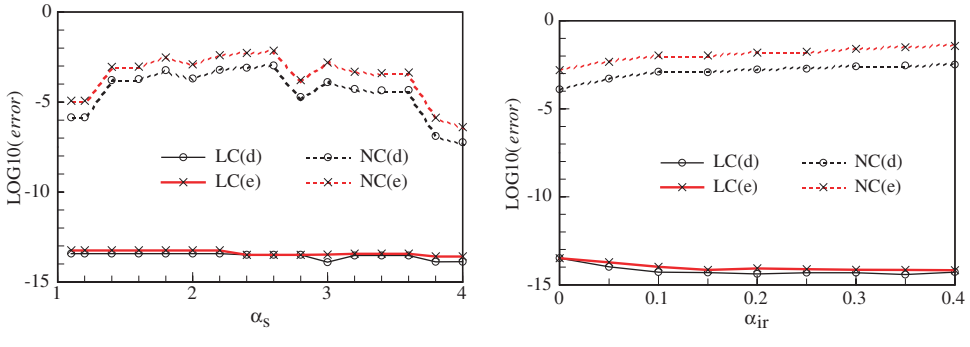


(a) (b)

Fig. 4. Relative error in the standard patch tests using NC-RPIM ($\alpha_c = 4.0$, $q = 1.03$) and LC-RPIM ($\alpha_c = 0.1$, $q = 0.5$). (a) Effect of the dimension of the support domain $\alpha_s$ for regular nodes. (b) Effect of the nodal irregularity factor $\alpha_{ir}$ ($\alpha_s = 2.5$).

is shown that the relative displacement and energy accuracies of the proposed LC-RPIM are very stable with the magnitude of $10^{-14}$ within the machine accuracy regardless the size of the support domain. The NC-RPIM is less stable, and its accuracy of displacement is of the order of $10^{-7} \sim 10^{-8}$ depending on the size of the support domain, and it is about one order higher than its energy accuracy. For a fixed nodal support domain of $\alpha_{\mathrm{s}} = 2.5$, the computed relative displacement and energy errors are plotted in Fig. 4(b) with varying irregularity factor $\alpha_{\mathrm{ir}}$ for the inner nodes in the patch. It is clearly shown that the accuracy of both displacement and energy of the LC-RPIM is stable and much higher than those of NC-RPIM. For irregular nodal distribution, the displacement accuracy of the LC-RPIM is almost same as its energy accuracy and of order of $10^{-15}$. The displacement accuracy of NC-RPIM is one order higher than its energy accuracy that is of the order of $10^{-3} \sim 10^{-4}$. To improve the accuracy of NC-RPIM, larger support domain is needed.

Based on the above comparisons, it is confirmed that the presented LC-RPIM using the proper shape parameters in the MQ-RBF can pass the patch test, but the NC-RPIM cannot.

### 5.2. *Cantilever beam*

The LC-RPIM is now applied to analyze the deformation and stress of a cantilever beam. The beam is of length $l$ and height $2c$ subjected to parabolically distributed vertical force at the right end as shown in Fig. 5. The beam has a unit thickness and plane stress problem is considered. The analytical solution is available and can be found in a textbook by Timoshenko and Gooder [1970].

The analytical stress of the cantilever beam is given by

$$\begin{cases} \sigma_x = -\dfrac{P(l-x)y}{I} \\ \sigma_y = 0 \\ \tau_{xy} = \dfrac{P}{2I}(c^2 - y^2) \end{cases} \tag{53}$$

where the moment of inertia $I$ of the beam is given as $I = \frac{2}{3}c^3$.

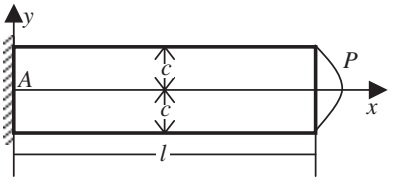


Fig. 5. Cantilever beam ($l = 8\,\mathrm{m}$, $c = 1\,\mathrm{m}$, $P = 1000\,\mathrm{kN}$).

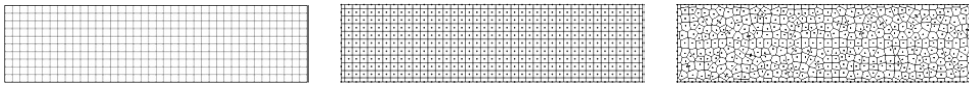

(a) (b) (c)

Fig. 6. A cantilever with 451 field nodes. (a) Background integration cells for NC-RPIM. (b) Nodal distribution and Voronoi diagrams for regular nodes. (c) Nodal distribution and Voronoi diagrams for irregular nodes ($\alpha_{\text{ir}} = 0.4$).

The analytical solution of the displacements of the beam is given by

$$\begin{cases} u = \dfrac{-Py}{2EI}\left[(2l-x)x + \dfrac{(2+\nu)}{3}(y^2 - c^2)\right] \\ v = \dfrac{P}{2EI}\left[v(l-x)y^2 + \left(l - \dfrac{1}{3}x\right)x^2 + \dfrac{(4+5\nu)}{3}c^2 x\right] \end{cases} \tag{54}$$

In the numerical computation, the parameters are taken as $E = 1.0 \times 10^4\,\text{MPa}$, $\nu = 0.25$, $l = 8\,\text{m}$, $c = 1\,\text{m}$ and $P = 1000\,\text{kN}$. Figure 6 illustrates background cells for NC-RPIM, the nodal distribution and its corresponding Voronoi diagrams for LC-RPIM with both regular and irregular nodes. For the case of irregular nodes, all the interior nodes except those on $x = 4$ and $y = 0$ are shifted according to Eq. (52) for a given $\alpha_{ir}$.

### 5.2.1. *Convergence study*

In this investigation, the dimension of the support domain is fixed at 2.5 and both regular and irregular ($\alpha_{\text{ir}} = 0.2$) nodes are used. Numerical results of relative displacement and energy errors calculated using different nodal spacing (averaged) are plotted in Fig. 7. It is numerically validated that the displacement and energy converge for both LC-RPIM and NC-RPIM. The accuracy and convergence rate in terms of energy norm of the present LC-RPIM is much higher than those of the NC-RPIM for both regular and irregular nodes. However, the displacement accuracy of the LC-RPIM is lower than that of NC-RPIM. This is because both methods are all based on the Galerkin weak form of assumed displacements, which minimizes the potential energy. As LC-RPIM guarantees the linear conformance of the displacements, the evaluation of the energy is accurate. On the other hand, the evaluation of the energy in NC-RPIM is "approximated" due to the non-conforming nature. Therefore, the energy error in LC-RPIM results is lower than that of NC-RPIM. However, the "relaxation" on the displacement conformance, gives the NC-RPIM a *chance* to produce better displacement solution. The situation is very similar to the well-known comparison between the conforming FEM and non-conforming FEM.

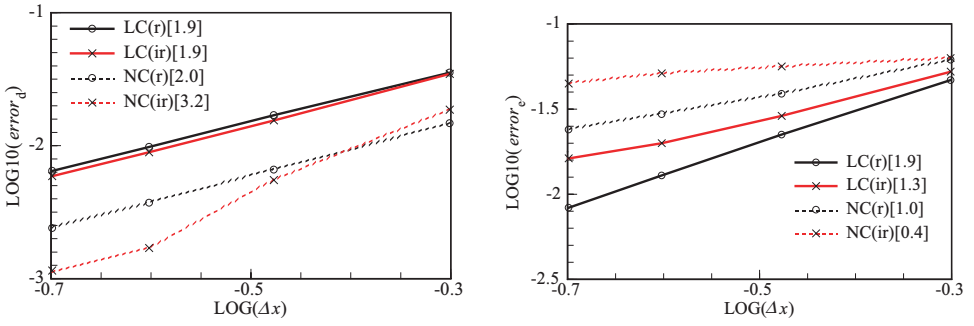


(a) (b)

Fig. 7. Convergence comparison for the cantilever beam solved using NC-RPIM and LC-RPIM with regular and irregular ($\alpha_{\text{ir}} = 0.2$) nodes ($\alpha_{\text{s}} = 2.5$), the numbers in square brackets are convergence rates. (a) Displacement. (b) Energy.

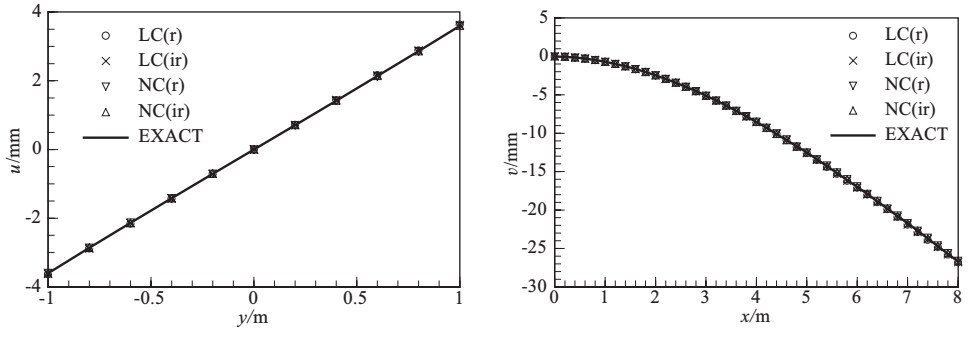


(a) (b)

Fig. 8. Displacement distribution along middle section ($x = \frac{1}{2}l$) and neutral axis ($y = 0$) obtained using NC-RPIM and LC-RPIM with regular and irregular ($\alpha_{\text{ir}} = 0.2$) nodes ($\alpha_{\text{s}} = 2.5$). (a) Horizontal displacement $u$. (b) Vertical displacement $v$.

### 5.2.2. *Comparisons of displacement and stress*

In this investigation, both regularly and irregularly (given $\alpha_{ir} = 0.2$) distributed nodes are used with the support domain $\alpha_{\text{s}} = 2.5$. The displacements along middle section and defections along neutral axis are shown in Fig. 8. The results of the two methods are found in good agreement with the analytical results. The stress $\sigma_x$ along middle section and stress $\tau_{xy}$ along neutral axis are shown in Fig. 9. It is clearly shown that the stresses obtained by the LC-RPIM are in much better agreement with the exact results than those of the NC-RPIM, especially for the case of irregular nodes.

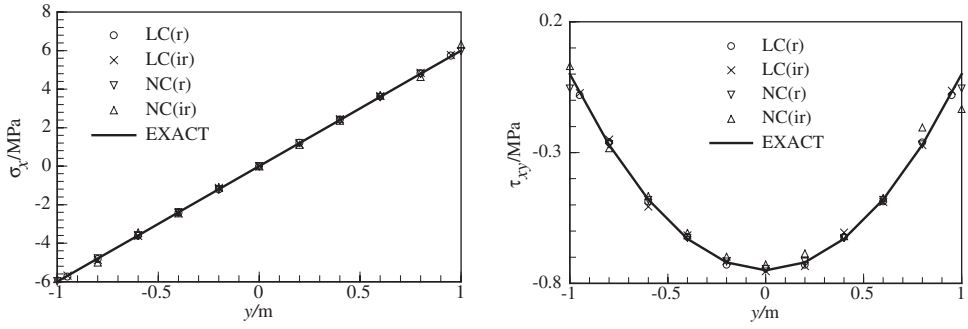


(a) (b)

Fig. 9. Stress distribution along middle section ($x = \frac{1}{2}l$) obtained using NC-RPIM and LC-RPIM with regular and irregular ($\alpha_{\text{ir}} = 0.2$) nodes ($\alpha_{\text{s}} = 2.5$). (a) Horizontal stress $\sigma_x$. (b) Shear stress $\tau_{xy}$.

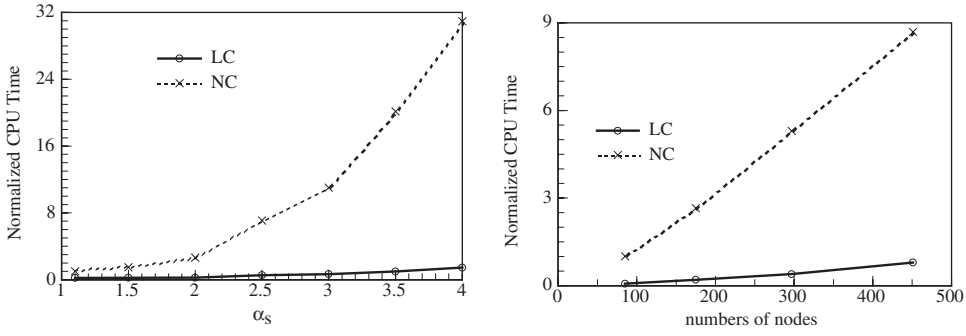


(a) (b)

Fig. 10. Comparison of CPU time (excluding solving the system equation) for LC-RPIM and NC-RPIM with regular nodes. (a) Effect of the dimension of the support domain using 297 regular nodes (normalized by the CPU time of NC-RPIM for $\alpha_{\text{s}} = 1.1$). (b) Effect of the number of nodes (normalized by the computing time of NC-RPIM with 85 nodes, $\alpha_{\text{s}} = 2.5$).

### 5.2.3. *CPU time comparison*

In this investigation, nodes are regularly distributed, and the CPU time excluding solving the system equation is considered. This is because the CPU times for solving the system equation are the same for both LC-RPIM and NC-RPIM. First, the number of nodes is fixed at 297, the CPU times of LC-RPIM and NC-RPIM are normalized against the CPU time of NC-RPIM for the support domain of $\alpha_{\text{s}} = 1.1$ as plotted in Fig. 10(a). It is shown that LC-RPIM is more efficient than NC-RPIM especially for larger support domain. Next, the dimension of the support domain is fixed at $\alpha_{\text{s}} = 2.5$ and the CPU times obtained for both methods are normalized with respect to the CPU time of NC-RPIM with 85 nodes and plotted in Fig. 10(b). It is also shown that the LC-RPIM is more efficient than NC-RPIM in term of the same nodes used.

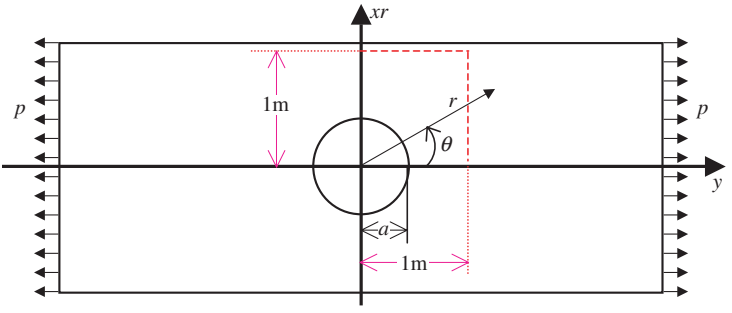


Fig. 11. Infinite plate with a circular hole ($a = 0.2\,\text{m}$, $p = 1\,\text{MPa}$).

### 5.3. *Infinite plate with a circular hole*

We now study the deformation and stress in a plate with a central circular hole of radius $a = 0.2\,\text{m}$ subjected to a unidirectional tensile load of $S = 1\,\text{MPa}$ in the $x$ direction, as shown in Fig. 11. Due to the symmetry, only the upper right quadrant of the plate with the size of $1\,\text{m} \times 1\,\text{m}$ is modeled. Plane stress problem is considered, and the material parameters used are $E = 10^4\,\text{MPa}$ and $\nu = 0.25$. Symmetry conditions are imposed on the left and the bottom edges of the quarter model and the inner arc boundary of the hole is traction free. The background cells, nodal locations and their Voronoi diagrams are illustrated in Fig 12. The interior nodal coordinates for relatively more irregular distribution are computed using the following equation.

$$\begin{cases} x' = x + L_{\min} r_{\text{R}} \cos(\pi r_\theta) \cdot \alpha_{\text{ir}} \\ y' = y + L_{\min} r_{\text{R}} \cos(\pi r_\theta) \cdot \alpha_{\text{ir}} \end{cases} \tag{55}$$

where $L_{\min}$ is the shortest distance of the node to its neighbor nodes, $r_R$ and $r_\theta$ are random numbers between $-1.0$ to $1.0$ produced by computer, and $\alpha_{\text{ir}}$ is the irregularity factor.

The analytical stress in the plate is given in the polar coordinate [18]:

$$\begin{cases} \sigma_r = \dfrac{p}{2}\left[\left(1 - \dfrac{a^2}{r^2}\right) + \left(1 - 4\dfrac{a^2}{r^2} + 3\dfrac{a^4}{r^4}\right)\cos 2\theta\right] \\ \sigma_r = \dfrac{p}{2}\left[\left(1 + \dfrac{a^2}{r^2}\right) - \left(1 + 3\dfrac{a^4}{r^4}\right)\cos 2\theta\right] \\ \tau_{r\theta} = -\dfrac{p}{2}\left(1 + 2\dfrac{a^2}{r^2} - 3\dfrac{a^4}{r^4}\right)\sin 2\theta \end{cases} \tag{56}$$

where $\theta$ is measured counterclockwise from the positive $x$-axis.

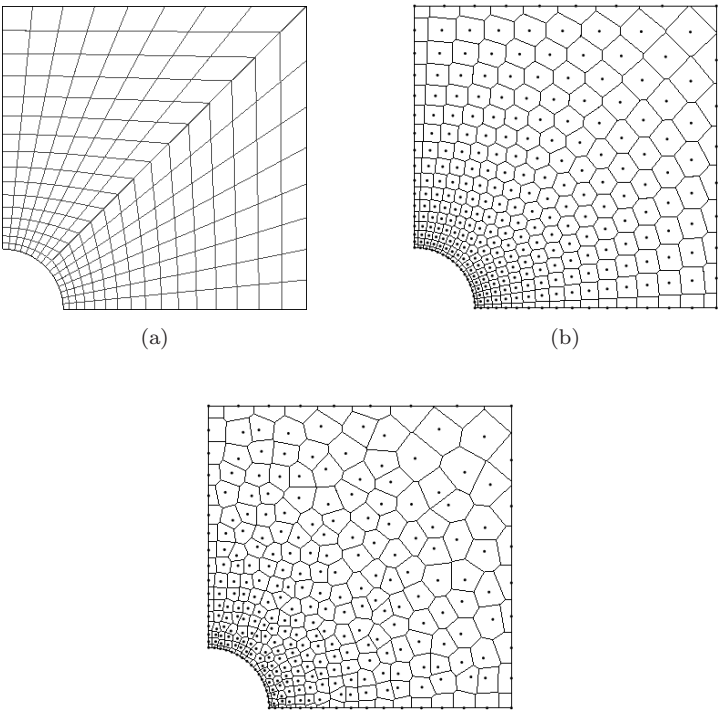


Fig. 12. Quarter model of an infinite plane with a circular hole. (a) Background integration cells for NCRPIM. (b) Regular nodes and Voronoi diagrams. (c) Irregular nodes and Voronoi diagrams ($\alpha_{\text{ir}} = 0.4$).

Similarly, the analytical displacement of the plate is given as

$$\begin{cases} u = \dfrac{rp}{2E}\left\{\left[(1-\nu)+(1+\nu)\dfrac{a^2}{r^2}\right]+\left[(1+\nu)+4\dfrac{a^2}{r^2}-(1+\nu)\dfrac{a^4}{r^4}\right]\cos 2\theta\right\} \\ v = -\dfrac{rp}{2E}\left[(1+\nu)+(1-\nu)\dfrac{2a^2}{r^2}+(1+\nu)\dfrac{a^4}{r^4}\right]\sin 2\theta \end{cases} \tag{57}$$

Traction boundary conditions given by the analytical solution in Eq. (54) are imposed along the right ($x = 1$) and the top ($y = 1$) edges.

5.3.1. *Convergence study*

In this investigation, the dimension of support domain is fixed at $\alpha_{\text{s}} = 2.5$. The relative errors of the displacement and energy obtained using LC-RPIM and NC-RPIM are plotted in Fig. 13 using different nodal spacing. It is numerically verified that the displacement and energy are convergent, and their convergence rate are

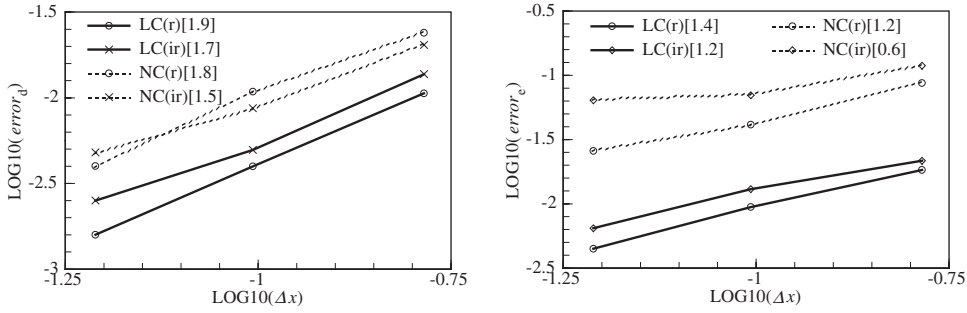


Fig. 13. Convergence of the solution for an infinite plate with a circular hole obtained using NC-RPIM and LC-RPIM with regular and irregular ($\alpha_{\text{ir}} = 0.4$) nodes ($\alpha_{\text{s}} = 2.5$), the numbers in square brackets are convergence rates. (a) Displacement. (b) Energy.

about the same. The accuracy of the LC-RPIM is much higher than that of the NC-RPIM. In addition, the nodal irregularity has a little effect on the accuracy and convergence rate.

### 5.3.2. *Comparisons of displacement and stress*

In this investigation, two dimensions of the support domain of $\alpha_{\text{s}} = 2$ and $\alpha_{\text{s}} = 3$ are used for the regular nodes. Figure 14 illustrates the horizontal displacement along $x$-axis, vertical displacement along $y$-axis and radial displacement along inner arc surface obtained using both LC-RPIM and NC-RPIM. It is clearly observed that the displacements of LC-RPIM are in better agreement with exact results than those of NC-RPIM. The stress $\sigma_y$ along $x$-axis, stress $\sigma_x$ along $y$-axis and stress $\sigma_\theta$ along inner arc surface are calculated and plotted in Fig. 15. It is seen again that stresses obtained by the LC-RPIM are also in better agreement with the analytical solutions compared to NC-RPIM. The results show also that the dimension of the support domain has little effect on displacement and stress obtained using LC-RPIM.

## 5.4. *Semi-infinite plate*

We now study a semi-infinite plane subjected to a uniform pressure loading over $[-a, a]$, as shown in Fig. 16(a). Plane strain problem is considered, and the analytical solution of the stress is given by

$$\begin{cases} \sigma_x = \dfrac{p}{2\pi}[2(\theta_1 - \theta_2) - \sin 2\theta_1 + \sin 2\theta_2] \\ \sigma_y = \dfrac{p}{2\pi}[2(\theta_1 - \theta_2) + \sin 2\theta_1 - \sin 2\theta_2] \\ \tau_{xy} = \dfrac{p}{2\pi}[\cos 2\theta_1 - \cos 2\theta_2] \end{cases} \tag{58}$$

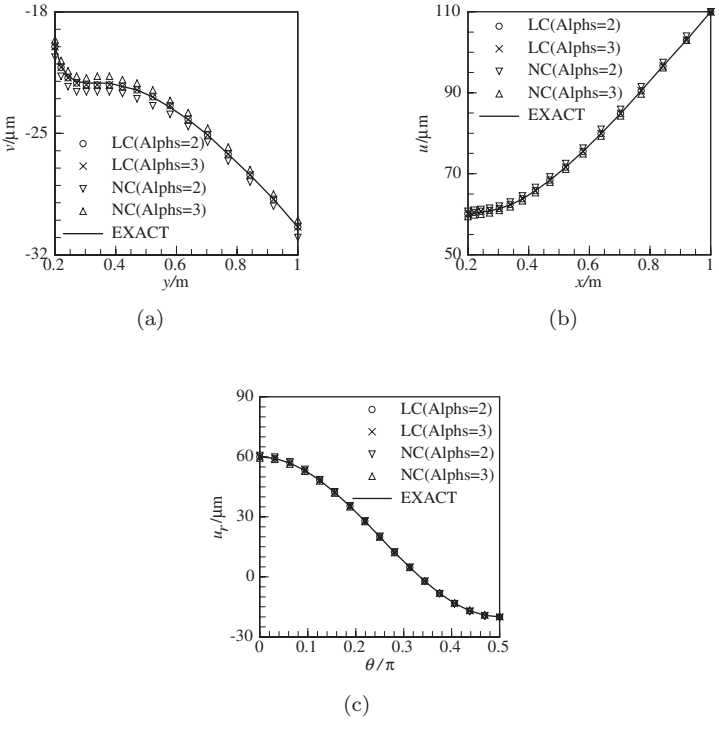


Fig. 14. Displacement distribution in an infinite plate with a circular hole obtained using NC-RPIM and LC-RPIM using regular nodes and different dimensions of the support domain. (a) $u$ along $x$-axis. (b) $v$ along $y$-axis. (c) $u_r$ along inner arc surface.

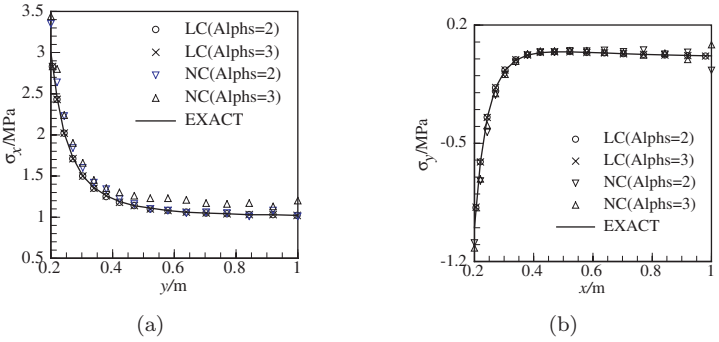


Fig. 15. Stress distribution in an infinite plate with a circular hole obtained using NC-RPIM and LC-RPIM using regular nodes and different dimensions of the support domain. (a) $\sigma_x$ along $y$-axis. (b) $\sigma_y$ along $x$-axis. (c) $\sigma_\theta$ along inner arc surface (EXACT(1) and EXACT(2) represent the values along the inner arc surface and the centroid of Voronoi diagrams of nodes along the inner surface, respectively).

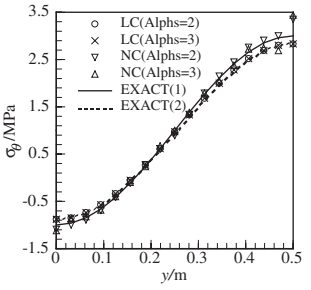


(c)

Fig. 15. (*Continued*)

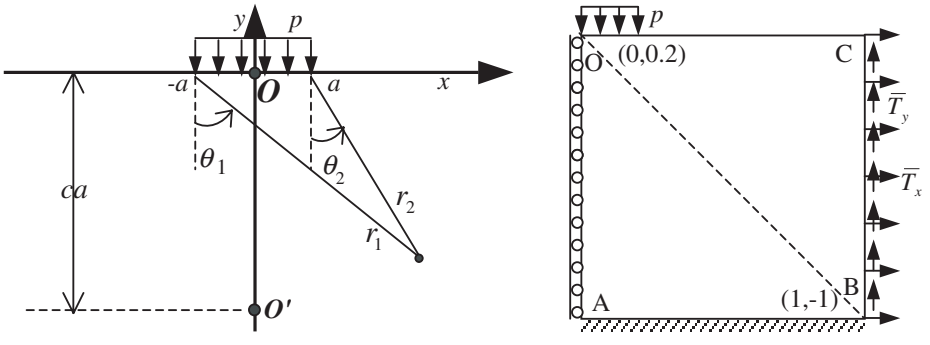


(a) (b)

Fig. 16. Semi-infinite plane subjected to an uniform pressure. (a) Configuration and coordinates. (b) Computation model ($a = 0.2$ m, $c = 100$, $p = 1$ MPa).

The analytical solution of displacement for the plane stress is given by

$$\begin{cases} u = \dfrac{p(1-\nu^2)}{\pi E}\left\{\dfrac{1-2\nu}{1-v}[(x+a)\theta_1 - (x-a)\theta_2] + 2y\ln\dfrac{r_1}{r_2}\right\} \\ v = \dfrac{p(1-\nu^2)}{\pi E}\left\{\dfrac{1-2\nu}{1-v}\left[y(\theta_1-\theta_2) + 2ca\left(\arctan\dfrac{1}{c}\right)\right] + 2(x-a)\ln r_2 \right. \\ \qquad \left. - 2(x+a)\ln r_1 + 2a\ln(a^2(1+c^2))\right\} \end{cases} \tag{59}$$

where $a$ is a half width applied pressure, an $c$ is a coefficient. $ca$ is the distance from the origin to the point $O'$ where the vertical displacement is assumed to be zero, as shown in Fig. 16(a).

Taking advantage of symmetry about the $y$-axis, the problem is modeled with a $5a \times 5a$ square of $a = 0.2$ m, as shown in Fig. 16(b), and coefficient $c$ is fixed at 100.

On the boundary of symmetry ($y = 0$), the displacement in the $x$-direction is fixed, while on the bottom boundary ($y = -1$) the displacements are prescribed using Eq. (59). Similarly on the right boundary ($x = 1$) the tractions computed using Eq. (58) are applied. Material parameters used in computation are $E = 100\,\text{MPa}$ and $v = 0.3$. The computational background cells, nodal distribution and Voronoi diagrams are shown in Fig. 17.

### 5.4.1. *Convergence comparison*

In this investigation, regularly distributed nodes are used, and the dimension of the nodal support domain used is $\alpha_s = 2.0$ and $\alpha_s = 3.0$. The relative errors of both displacement and energy are calculated using both LC-RPIM and NC-RPIM as plotted in Fig. 18, with the change of the average nodal spacing. It is observed again that these two methods converge at about the same rate regardless of the dimension of the support domain. The displacement accuracy for the NC-RPIM is

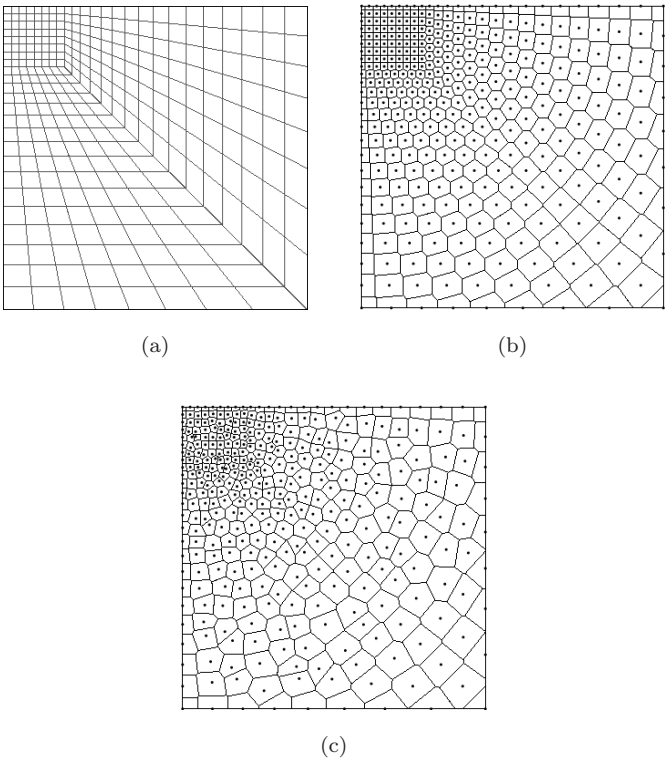


Fig. 17. (a) Background integration cells for NC-RPIM. (b) Regular nodes and Voronoi diagrams. (c) Irregular nodes and Voronoi diagrams ($\alpha_{ir} = 0.4$).

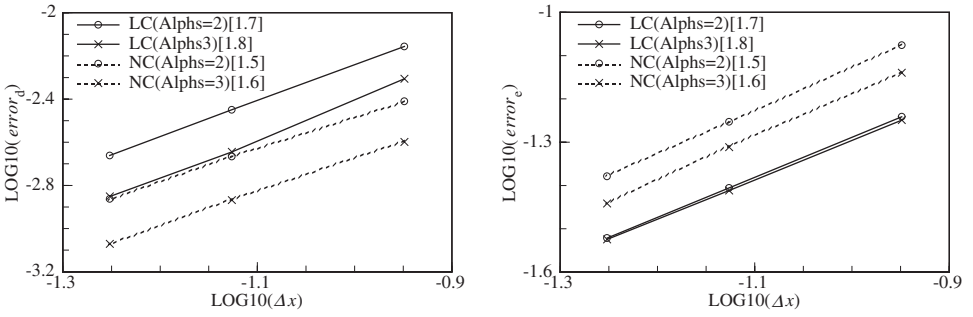


Fig. 18. Convergence of solution for the semi-infinite plane problem obtained using NC-RPIM and LC-RPIM with different support domains, the numbers in square brackets are convergence rates. (a) Displacement. (b) Energy.

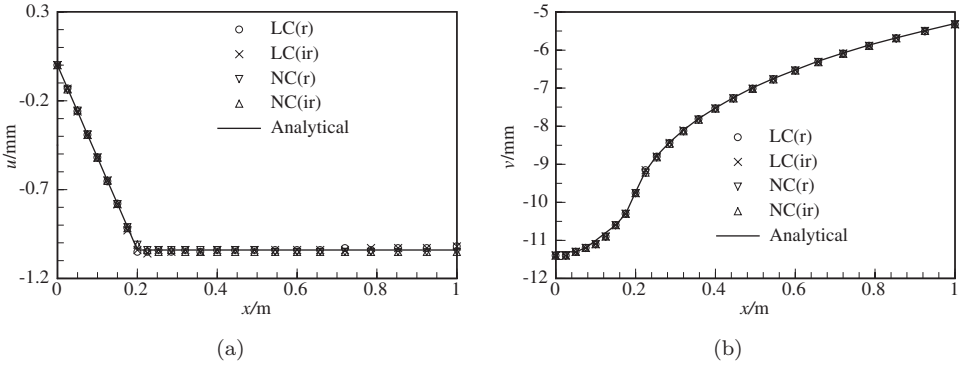


Fig. 19. Displacement distribution along free surface of the semi-infinite plane problem obtained using NC-RPIM and LC-RPIM with regular and irregular ($\alpha_{\rm ir} = 0.4$) nodes ($\alpha_{\rm s} = 2.5$). (a) Horizontal displacement $u$. (b) Vertical displacement $v$.

higher than that of LC-RPIM, however the accuracy in terms of the energy norm for the LC-RPIM is higher than that of NC-RPIM.

### 5.4.2. *Comparisons of displacement and stress*

In this investigation, both regularly and irregularly ($\alpha_{\rm ir} = 0.4$) distributed nodes are used with the support domain of $\alpha_{\rm s} = 2.5$. The displacements computed along upper free surface are plotted in Fig. 19. It is shown that the results of the two methods are in good agreement with the analytical results. The stresses calculated along the diagonal line (O-B) are plotted in Fig. 20. It is clearly observed that the stresses obtained by the presented LC-RPIM coincide better with the analytical solutions than those of NC-RPIM, especially for irregular nodes and near the boundary. This shows again that the LC-RPIM is less sensitive to nodal irregularity.

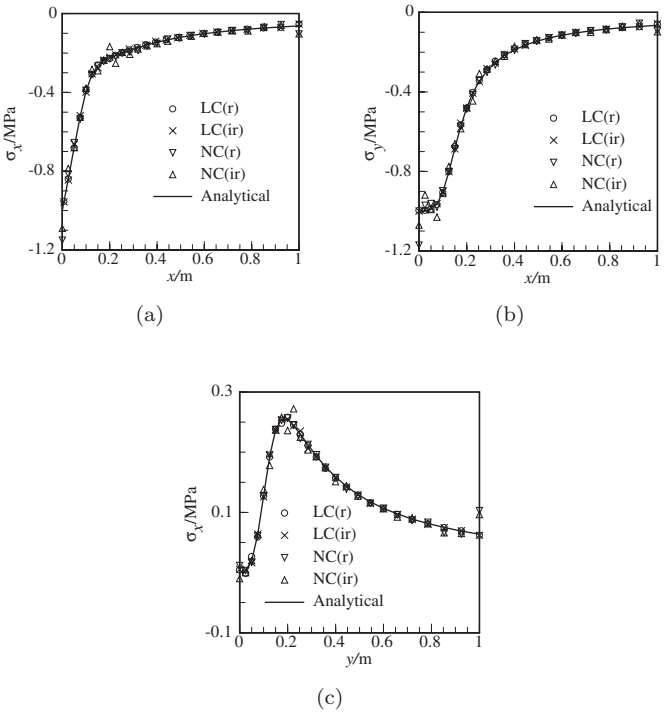


Fig. 20. Stress distribution along the diagonal line (O-B) of the semi-infinite plane problem obtained using NC-RPIM and LC-RPIM with regular and irregular ($\alpha_{\rm ir} = 0.4$) nodes ($\alpha_{\rm s} = 2.5$). (a) $\sigma_{xx}$ (b) $\sigma_{yy}$ (c) $\tau_{xy}$.

### 5.5. *Triangular plate with a heart-shaped hole*

To examine the capability of LC-RPIM for problem with very irregular configuration, we now study the deformation and stress of a triangular plate with a heart-shaped hole subjected to a unilateral uniform pressure of $p = 1.0\,\text{MPa}$, as shown in Fig. 21. Plane stress problem is considered, and the material of $E = 10^4\,\text{MPa}$ and $\nu = 0.25$ is used in computation. The background cells for NC-RPIM, nodal distribution (962 nodes) and Voronoi diagrams are shown in Fig. 22. Since there is no analytical solution for this problem, the problem is analyzed using FEM software ABAQUS with a large number of (8140) nodes so that the results can be used as a reference solution for comparison purpose.

In this investigation, three dimensions of the support domain are used: $\alpha_{\rm s} = 1.5, 2.5$ and $3.5$. The displacement computed using these different methods is plotted in Fig. 23, and the stress along $y$ axis on the heart-shaped tip (D-C) is also pictured in Fig. 24. It is clearly shown that the displacement and stress obtained by LC-RPIM are more stable and agree better with those of FEM compared to NC-RPIM. Note that NC-RPIM gives very good results when $\alpha_{\rm s} \geq 2.5$, as suggested by Liu [2003].

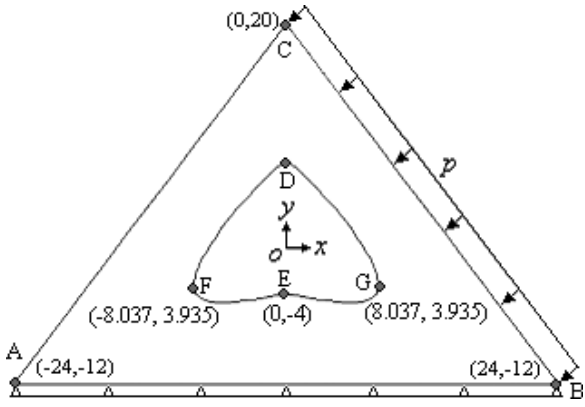


Fig. 21. Triangular plate with a heart-shaped hole, which is consisted of two splines through D-F-E and D-G-E, respectively, subjected to unilateral uniformed pressure (All dimension is meters).

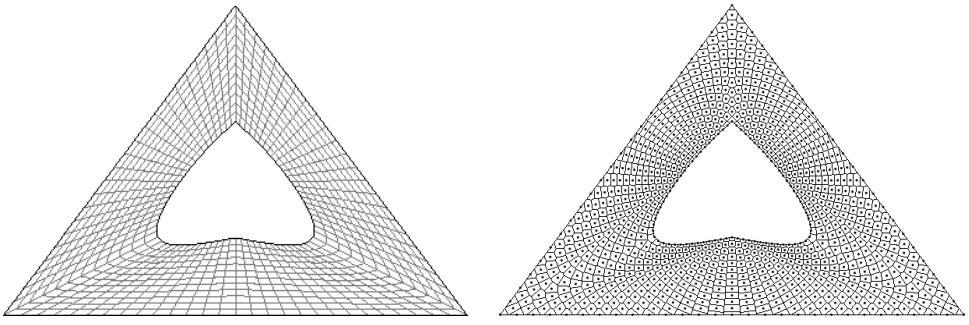

(a) (b)

Fig. 22. Triangular plate with a heart-shaped hole. (a) Background integration cells for NC-RPIM (b) Nodal collection and Voronoi diagrams for LC-RPIM.

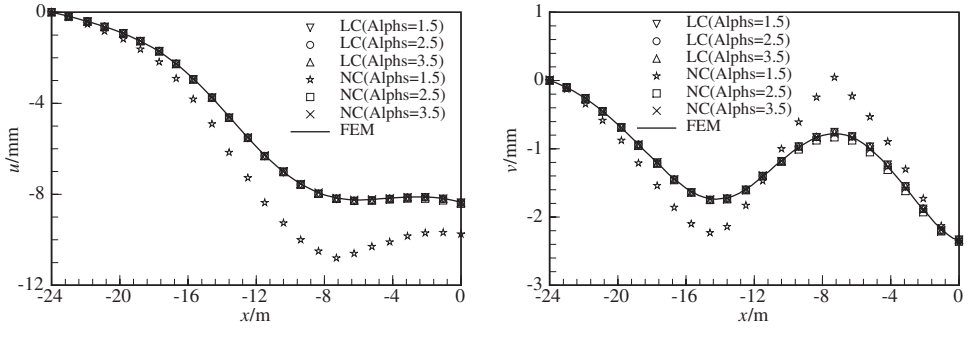


(a) (b)

Fig. 23. Effect of the equivalent nodal spacing on displacement distribution along free boundary (A-C) of the triangular plate with a heart-shaped hole obtained using NC-RPIM and LC-RPIM. (a) Horizontal displacement $u$. (b) Vertical displacement $v$.

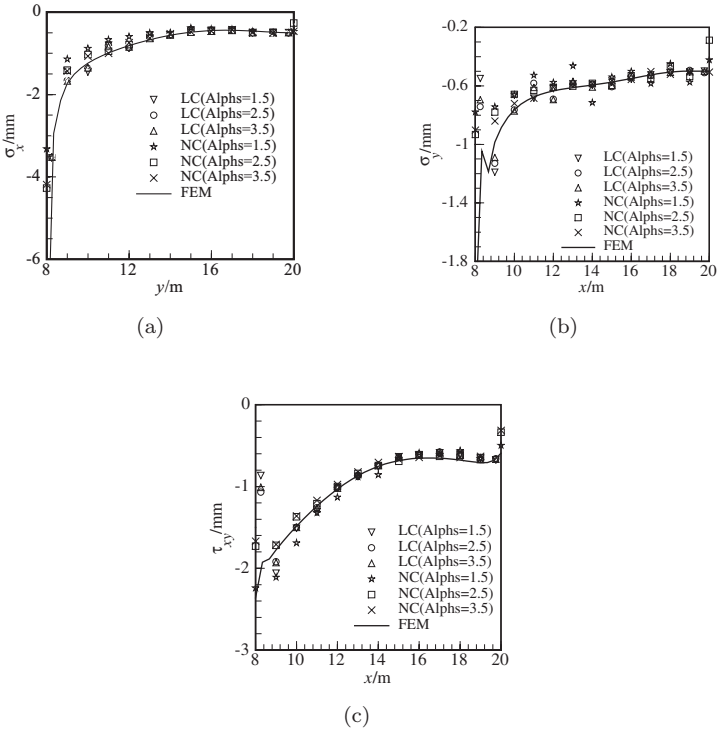


Fig. 24. Effect of the equivalent nodal spacing on stress distribution along the vertical line (D-C) of the triangular plate with a heart-shaped hole obtained using NC-RPIM and LC-RPIM. (a) $\sigma_{xx}$ (b) $\sigma_{yy}$ (c) $\tau_{xy}$.

## 6. Conclusion

A linearly conforming radial point interpolation method (LC-RPIM) is presented in this work based on nodal integration. In this method, each node is enclosed by a Voronoi polygon. The conformability is restored by (a) using RPIM shape functions with at least complete linear consistency; (b) the gradient is averaged over the smoothing domain leading to constant strain for the nodal integration. The essential boundary is imposed directly as in the FEM.

Compared with NC-RPIM, the LC-RPIM has been found to have the following advantages:

(1) The LC-RPIM can accurately reproduce linear displacement field. The method can achieve the linear convergence rate, which is about 2.0 for displacement and 1.0 for energy as demonstrated in examples.
(2) More stable and accurate in stress than NC-RPIM. The computed results of LC-RPIM are less susceptible to the dimension of the support domain and the nodal irregularity compared to NC-RPIM.
(3) The LC-RPIM using nodal integration is generally more efficient than the original RPIM using Gaussian integration.

## References

Atluri, S. N. and Zhu, T. [1998] "A new meshless local Petrov–Galerkin (MLPG) approach in computational mechanics," *Comput. Mech.* **22**, 117–127.

Atluri, S. N., Cho, J. Y. and Kim, H. G. [1999] "Analysis of the thin beam, using the meshless local Petrov–Galerkin (MLPG) method, with generalized moving least squares interpolations," *Comput. Mech.* **24**, 334–347.

Belytschko, T., Lu, Y. Y. and Gu, L. [1994] "Element-free Galerkin methods," *Int. J. Num. Methods Eng.* **37**, 229–256.

Belytschko, T., Krongauz, Y., Organ, D., Fleming, M. and Krysl, P. [1996] "Meshless methods: An overview and recent developments," *Comput. Methods Appl. Mech. Eng.* **137**, 3–47.

Bonet, J. and Kulasegaram, S. [2002] "A simplified approach to enhance the performance of smooth particle hydrodynamics methods," *Appl. Math. Comput.* **126**, 133–155.

Chen, J. S., Wu, C. T., Yoon, S. and You, Y. [2001] "A stabilized conforming nodal integration for Galerkin mesh-free methods," *Int. J. Num. Methods Eng.* **50**, 435–466.

Chen, J. S., Yoon, S. and Wu, C. T. [2002] "Non-linear version of stabilized conforming nodal integration for Galerkin mesh-free methods," *Int. J. Num. Methods Eng.* **53**, 2587–2615.

Gingold, R. A. and Monaghan, J. J. [1977] "Smoothed particle hydrodynamics: Theory and application to non-spherical stars," *Month. Not. Royal Astro. Soc.* **181**, 375–389.

Golberg, M. A., Chen, C. S. and Karur, S. R. [1996] "Some recent results and proposals for the use of radial basis functions in the BEM," *Eng. Anal. Bound. Ele.* **18**, 9–17.

Liu, W. K., Jun, S., and Zhang, Y. F. [1995] "Reproducing kernel particle methods," *Int. J. Num. Methods Fluids* **20**, 1081–1106.

Liu, G. R. and Gu, Y. T. [2001] "A point interpolation method for two-dimensional solid," *Int. J. Num. Methods Eng.* **50**, 937–951.

Liu, G. R. [2003] *Meshfree Methods, Moving Beyond the Finite Element Method* (CRC Press Publication).

Liu, G. R. and Gu, Y. T. [2005] *An Introduction to Meshfree Methods and Their Programming* (Springer).

Lucy, L. B. [1977] "A numerical approach to the testing of fusion process," *Astro. J.* **88**, 1013–1024.

Lu, Y., Belytschko, T. and Gu, L. [1994] "A new implementation of the element-free Galerkin method," *Comput. Methods Appl. Mech. Eng.* **133**, 397–414.

Randles, P. W. and Libersky, L. D. [1996] "Smoothed particle hydrodynamics: Some recent improvements and applications," *Comput. Methods Appl. Mech. Eng.* **139**, 375–408.

Timoshenko, S. P. and Goodier, J. N. [1970] *Theory of Elasticity*, 3rd edition (McGraw-Hill: New York).

Wang, J. G. and Liu, G. R. [2002] "On the optimal shape parameters of radial basis functions used for 2-D meshless methods," *Comput. Methods Appl. Mech. Eng.* **191**, 2611–2630.